



In-Flight Measurements of Particle Temperature and Velocity with a High-Speed IR Camera During Cold Gas Spraying of In718 and TiAlCrNb

Jochen Fiebig¹ · Jean-Phillipe Gagnon² · Georg Mauer¹ · Emine Bakan¹ · Robert Vaßen¹

Submitted: 14 February 2022 / in revised form: 25 April 2022 / Accepted: 18 May 2022
© The Author(s) 2022

Abstract Unlike other thermal spraying methods, it is difficult to determine the temperature of the particles during cold gas spraying due to the relatively low radiation. In the present study, the velocities and in-flight temperatures of metal particles were measured during cold gas spraying. A state-of-the-art high-speed infrared camera was used to study the behavior of two different base materials, In718 and TiAlCrNb, both used as structural materials in gas turbine engines. The experiments aimed to improve the fundamental understanding of the process, in particular the heating of the particles, and to compare the experimental results with theoretical calculations of the particle temperatures.

Keywords cold spray · cold spray meter · infrared camera · particle temperature · particle velocity

Introduction

Cold gas spraying is a promising method for additive manufacturing and repair applications in the aerospace industry. In contrast to other thermal spray techniques the relatively low process temperatures offer several advantages, (i) minimization of oxidation, (ii) low thermal stress,

and (iii) prevention of unwanted (or unintended) phase transformations (Ref 1, 2).

Reliable predictions for successful bonding in cold gas spray have been investigated for around 20 years. A simple equation for the required critical velocity depending on certain material properties (density, yield stress, melting temperature) as well as the initial particle temperature was given by Assadi et al. in 2003 (Ref 3). Further improvements on this approach were done by Schmidt et al. (Ref 4, 5) who developed a general window of deposition for the cold gas spray process. In their work, an equation for the critical velocity depending on particle impact temperature, and the properties of the feedstock material, namely density, heat capacity, and yield strength, was derived (Ref 5). In addition, Schmidt et al. also investigated the influence of the particle size on the critical velocity and gave simple dependencies for Cu and 316L steel (Ref 5). A new dimensionless parameter η (ratio of particle impact velocity and critical velocity) was introduced by Assadi et al. (Ref 6) and so-called parameter selection maps were developed to simplify the determination of reasonable conditions for the experiments. It should be noted that the critical velocity in their study is still based on the description by Schmidt et al. (Ref 5). An alternative description to the parameter selection map is the so-called cold spray coating diagram (CSCD) introduced by Kamaraj and Radhakrishnan (Ref 7). Here, the ratio of particle temperature and melting temperature (T_p/T_m) is plotted against the particle velocity v_p . By including available experimental data, e.g., adhesion strength or deposition efficiency, and the experimentally observed bonding mechanisms, e.g., surface melting or adiabatic shear instability, a complete picture of the material dependent coating diagram can be created. During the past 10 to 15 years, alternative models for the critical velocity and the bonding process have been developed by,

✉ Jochen Fiebig
j.fiebig@fz-juelich.de

¹ Forschungszentrum Jülich GmbH, Institute of Energy and Climate Research, Materials Synthesis and Processing (IEK-1), 52428 Jülich, Germany

² Telops Innovative Infrared Imaging, 100-2600 Jean-Baptiste Avenue, Quebec City, Canada

e.g., Li et al. (Ref 8) and Hassani-Gangaray et al. (Ref 9). The latter authors suggest based on their experimental in situ impact observations (Ref 10) that adiabatic shear instability is not necessary for the bonding in cold gas spray. As an alternative, a hydrodynamic description of the process is developed and a relationship between the critical velocity and the bulk speed of sound is derived (Ref 9). Yet, in most of these models, the particle impact velocity and temperature are two key factors to describe the bonding behavior. Thus, it is essential to measure these physical quantities experimentally.

Consequently, high-quality particle diagnostics are indispensable for the comparison of known theoretical models with experimental observations and future developments toward industry 4.0. Progress in the field could lead to an improved fundamental understanding of the cold gas spray process and enable scientists to confirm, reject or refine existing models.

Several authors have demonstrated that particle velocities can be measured with different methods accurately in-flight using a laser-two-focus (L2F) (Ref 11), DPV-2000 or DPV-CPS (laser illumination) (Ref 12–17), CCD-camera (OESIR SprayWatch) (Ref 18–20), laser-illuminated particle velocimetry (Ref 21), particle image velocimetry (PIV) (Ref 22, 23), laser scattering (Ref 23), particle tracking velocimetry (PTV) (Ref 24–26) or sizing particle tracking velocimetry (S-PVT) (Ref 27), particle/droplet image analysis (PDIA) (Ref 28) or a cold spray meter (CSM) (Ref 29–33). In a CSM, a laser beam is aligned with the particle jet and the reflected laser light is detected by an optical sensor, typically an optical fiber. A double-slit mask is placed in front of the sensor head. As a consequence, a particle passing in front of the sensor will generate a double-peak signal. The time between the two peaks is the so-called time of flight (TOF) of the particles. With the known dimensions of the mask and magnification factor of the optics, it is possible to calculate the particle velocities. More details can be found in the literature (Ref 12, 13, 29)

Although the particle temperatures are used in the calculations of the critical velocity, see, e.g., (Ref 4–6), it is challenging to determine the particle temperatures experimentally in-flight which is related to the high particle velocities of 400–1200 m/s and simultaneously relatively low particle temperatures of a few hundred degrees. For this reason, the particle temperatures in cold gas spray are usually obtained by calculations using either simplified models (e.g., the isentropic model (Ref 4, 6)) or computational fluid dynamics simulations (CFD) (Ref 4, 5, 33–35). A comprehensive review on the modeling in cold gas spray was published by Yin et al. (Ref 36) comparing simplified numerical models with state-of-the-art CFD simulations and experimental results.

The temperature distribution inside a particle during cold gas spray is usually assumed to be uniform, since in most cases the Biot-number is smaller than 0.1. Katanoda (Ref 37) investigated cases where the particle temperature distribution is no longer uniform within the sprayed particles and found that for materials with low heat conductivities (e.g., Al_2O_3) a difference between the core and the surface temperature exist. In a more recent study Raelison et al. (Ref 38) analyzed the particle temperature distribution in cold sprayed particles in more detail and formulated a criterion for the uniformity of the particle temperature, named RUT_p (Ref 38). The criterion depends on gas velocity, particle size and the ratio of the thermal conductivities of the particle material and the process gas.

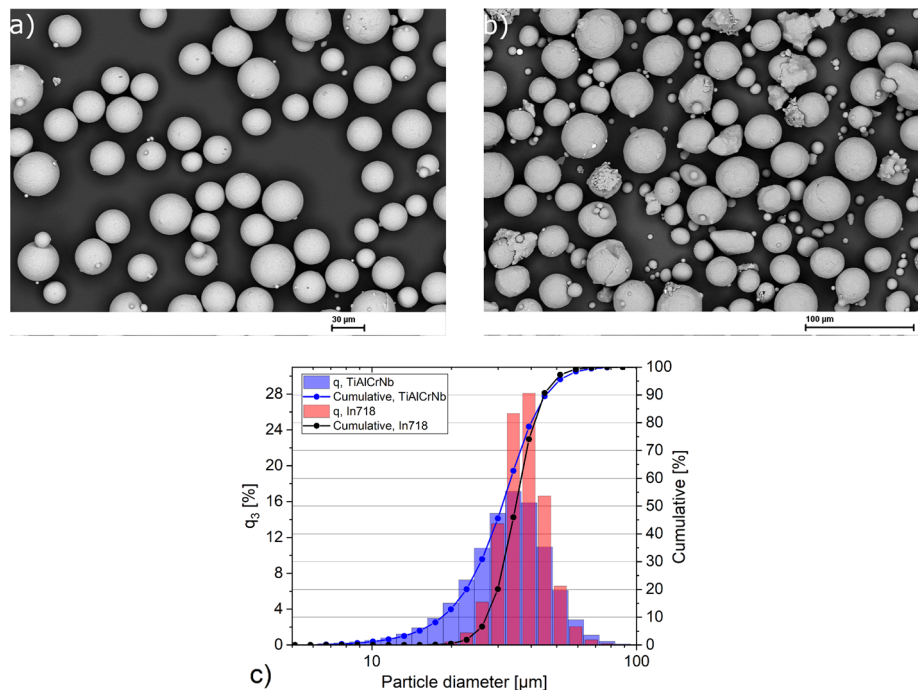
A first attempt to obtain particle temperatures experimentally in-flight during cold gas spray was undertaken by Nastic and Jodoin (Ref 33), who used a high-speed IR camera to analyze sieved Ti-particles with a diameter of around 150 μm . The highest temperature was assumed to be the particle temperature. Two different methods, particle streak velocimetry (PSV) and particle track velocimetry (PTV), were utilized to determine the particle velocities. In their study, the obtained particle velocities (below 200 m/s) and temperatures (less than 100 $^\circ\text{C}$) were below the necessary conditions for successful coating deposition, means outside of the deposition window.

In the present study, we will focus on in-flight particle diagnostics of Inconel 718 and TiAlCrNb (AE AlloysTM) particles that exceed the critical velocity and could be used for potential applications in future. For this purpose, a high-speed IR camera is used, an improved model compared to the one used by Nastic and Jodoin (Ref 33), and further details will be provided later. The influences of the emissivity and particle size on the particle temperature are discussed. The quality of the experimental results is evaluated by comparing the particle velocities and temperatures to predictions of the KSS software (Ref 39). Furthermore, for the IN718 feedstock, a comparison between the results of a cold spray meter (CSM) and those obtained by the IR camera is presented.

Experimental Methods and Data Analysis

Two different powders, In718 (Inconel 718) and TiAlCrNb (Ti-48Al-2Cr-2Nb), were used in the present study. The In718 powder was provided by AP&C (Canada) and the characteristic values for d_{10} , d_{50} , and d_{90} are 27, 35, and 45 μm , respectively. The second feedstock was a gas atomized TiAlCrNb powder customized for the cold gas spray process. The particle size of this powder was measured as $d_{10} = 17 \mu\text{m}$, $d_{50} = 32 \mu\text{m}$ and $d_{90} = 48 \mu\text{m}$ using the laser diffraction method (LA-950-V2, Horiba Ltd., Tokyo,

Fig. 1 SEM images and particle size distributions of the In718 and TiAlCrNb feedstock: (a) Morphology of In718, (b) Morphology of TiAlCrNb and (c) comparison of the particle size distributions and cumulative percentages of the feedstocks. The distributions are given in volume percent (Color figure online)



Japan). The spherical morphologies of the two feedstocks with some satellites at the particle surfaces and the particle size distributions are shown in Fig. 1(a), (b), and (c).

Figure 2 shows the IR camera (FAST M2K) and cold gas spray experimental setup used in this study. An impact 5/11 system (Impact Innovations GmbH, Rattenkirchen, Germany) was used for the cold spray experiments. The cold spray gun is equipped with a water-cooled SiC-D24 convergent-divergent De-Laval-nozzle. During the experiments, a gas inlet temperature of 1100 °C and a gas inlet pressure of 50 bar (N₂) were chosen. A further increase of the particle temperatures was achieved by attaching a longer pre-chamber with a length of 170 mm to the cold spray gun. As a result, the injected particles spend more time in the hot gas. The particle velocities are not affected by a longer pre-chamber length. For the experiments, the IR camera was focused at a spray distance of 60 mm. In the present study, there was no substrate in front of the cold spray gun, which avoids the bow shock effect.

As reported in (Ref 33), there are two methods to measure the velocities of the particles with an IR camera, namely particle tracking velocimetry (PTV) and particle streak velocimetry (PSV). In the PTV method, two consecutive frames are analyzed. The same particle has to be present in both frames and then the travel distance of this particle can be obtained from the measured starting and final position in the respective frames. With the known time between two consecutive frames (1/acquisition rate) the particle velocity can be calculated. Due to the low acquisition rate of 10 kHz the PTV method was not

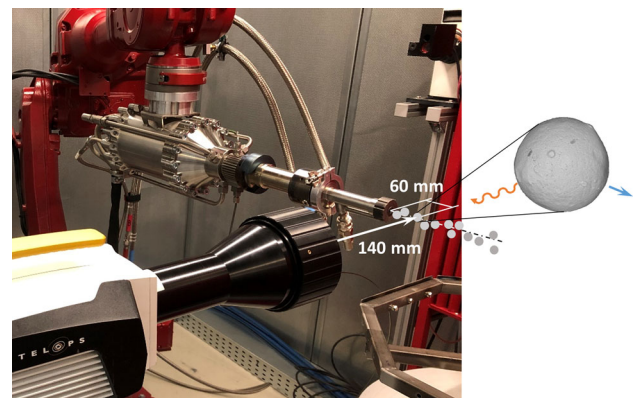


Fig. 2 Photograph of the experimental setup. In the front the high-speed IR camera from Telops is visible. In the background is the Impact 5/11 system equipped with the D24 converging-diverging DeLaval nozzle and the extended pre-chamber. Furthermore, the spraying distance of 60 mm and the distance of 140 mm between the lens and the particle beam are indicated. Schematically drawn are the flying particles and one particle is enlarged on the right side. The traveling direction of the particle (blue arrow) and the emitted infrared energy (orange curved line) are depicted (Color figure online)

applicable in the present study. The time between two frames is 100 µs and particles with a velocity of more than 400 m/s would fly through the entire field of view within that time interval. In the second method (PSV), the starting and final positions of the particles are determined in the same frame. During the exposure time of the image, the particles travel a certain distance and emit infra-red energy. The length of the “streak” of infrared energy is the travel distance of the particle, more precisely, the length of the

streak is the travel distance plus the particle diameter. Since the exposure time is known, 2 μs in the present work, the particle velocity could be calculated. In the present study, the PSV was used to determine the particle velocity distributions of In718 and TiAlCrNb. In the post-treatment of the In718 data, the particle velocities were filtered into 3 groups: (i) $v_1 < 400$ m/s, (ii) $400 \leq v_2 < 1000$ m/s and (iii) $v_3 \geq 1000$ m/s. The reason for the filtering will be discussed later in more detail (see Sect. “Results and Discussions”).

Nastic and Jodoin (Ref 33) also described the basics of the temperature measurements with an IR camera. The total infrared energy measured by the IR camera is a sum of three different contributions, (i) infrared energy emitted from the particle, (ii) infrared energy of the surroundings reflected by the surface of the particle, and (iii) the emitted infrared energy of the surrounding atmosphere (this contribution is neglected in the temperature calculations). As a result, a semi-empirical Planck law was derived that expresses the signal detected by the infrared camera [Eq 31 in (Ref 33)]:

$$W_{\text{tot}} = \varepsilon_{\lambda, T_p} \frac{R}{\exp\left(\frac{B}{T_p}\right) - F} + (1 - \varepsilon_{\lambda, T_p}) \frac{R}{\exp\left(\frac{B}{T_{\text{ref}}}\right) - F} \quad (\text{Eq 1})$$

here, ε stands for the emissivity (depending on wave-length of the measured signal and the particle temperature) of the particle material, T_p is the particle temperature, T_{ref} stands for the temperature of the surroundings, R is a function of integration time and wavelength band, B is a function of wavelength only ($B = hv/k_B$) and F is a positive value close to 1.

Therefore, for the particle temperature calculations, the spectral hemispherical emissivity value of the particles has to be known. Due to its use in the aerospace industry, nuclear reactors or cryogenic storage tanks the emissivity of In718 has been studied quite intensively (Ref 40–50). In the literature, usually values for the total hemispherical emissivity (Ref 40, 43, 47) or the spectral emissivity (directional, effective or normal) of In718 (Ref 41, 42, 44–46, 48–50) are given. Furthermore, it should be noted that the emissivity depends on several factors like surface roughness (Ref 41) or surface oxidation. Values for total hemispherical emissivity values of as-received In718 with a temperature of 700 to 1400 K lie between 0.2 and 0.3 (Ref 40). After oxidation or surface treatments like sand-blasting, the total hemispherical emissivity values increase up to 0.5 or 0.7, respectively (Ref 40). Based on these, the interval for the emissivity of In718 was chosen between 0.5 and 0.9. While the emissivity of In718 was reported extensively, no emissivity data could be found for TiAlCrNb alloy in the literature. Therefore, emissivity for

this alloy was chosen based on the studies reported on TiAl. Belskaya (Ref 51) measured emissivity of TiAl alloys with up to 10 at.% Al as 0.18 to 0.32 between 800–1400 K temperature range. It was suggested that the emissivity of the investigated titanium alloys depends weakly on the composition. Krishnan et al. (Ref 52) on the other hand determined emissivity of TiAl alloys with higher Al contents (40.3–95 at.%), which is closer to the composition investigated in this study, at near melting temperatures (1400–2000 K) and reported values between 0.10 to 0.34. In this study, in contrast to the work of Belskaya, the emissivity of TiAl alloys was found to exhibit nonlinear variations both with composition and temperature. In both studies, the measurements were made under vacuum or protective atmosphere implying that oxidation effects were not considered which leads to an increase in emissivity values. Therefore, a large emissivity range between 0.1–0.7 was used in the present work for the analysis of the TiAlCrNb measurement data collected by the IR camera.

The software of Telops requires the particle diameter as well as the emissivity to be chosen before running the analysis. Due to this limitation of the software, it was decided to use a fixed particle diameter of 30 μm and investigate the influence of the emissivity. For each chosen emissivity value the same particles were identified and analyzed by the software. This assumption enables a link between the particle temperatures of a particle of fixed size but with different emissivity values, i.e., the particle temperatures for lower or higher emissivity values can be extrapolated according to Eq 2:

$$T_{p2} = \frac{C_4}{\lambda} \left(\ln \left(\frac{\varepsilon_{p2}}{\frac{\varepsilon_{p2} - \varepsilon_{p1}}{\exp\left(\frac{C_4}{\lambda T_{\text{ref}}}\right) - 1} + \frac{\varepsilon_{p1}}{\exp\left(\frac{C_4}{\lambda T_{p1}}}\right) - 1}} + 1 \right) \right)^{-1} \quad (\text{Eq 2})$$

here, ε_{p1} and ε_{p2} are the emissivity values of a particle with temperatures T_{p1} and T_{p2} , respectively. Furthermore, C_4 and λ are constants ($C_4 = hc/k_B = 1.438775 \times 10^{-2}$ mK and $\lambda = 4$ μm , see (Ref 33)).

For comparison, the particle velocities were also measured with a cold spray meter (CSM) from Tecnar. A laser beam (wavelength 790 nm, power 3.3 W, divergence 70 mrad) is aligned with the particle beam and the reflected laser light is detected by an optical sensor which is equipped with a double-slit mask. Using the time of flight and the known dimensions (80 μm between the slits, width of the slits is 80 μm) of the mask the particle velocity is calculated with an accuracy in the order of 0.5%. For each experiment, 10,000 particles were evaluated. Furthermore, the particle diameters were estimated from the measured

energies assuming that the scattered radiation intensity corresponds to the surface area of a spherical particle. Before, a calibration coefficient has to be determined from a measurement of reference particles with a known volumetric mean particle diameter and the same emissivity. The particle size is obtained with an accuracy of 7–15%, and that it is greatly dependent on the validity of the hypothesis of sphericity of the particles.

During the experiments, several videos with around 100,000 frames were recorded and a smaller subset of around 21,500 frames was analyzed automatically for different pre-set parameters, e.g., particle radius, material emissivity, distance to the object, and surrounding conditions (e.g., humidity and temperature). An acquisition rate of 10 kHz and an exposure time of 2 μ s were chosen. The field of view was set to 320×40 pixels. Since the pixel size of the camera is $30 \times 30 \mu\text{m}$, the field of view has a size of $9.6 \times 1.2 \text{ mm}$.

Additionally, the KSS software was used to calculate the particle i temperatures and particle velocities from the injection point to the substrate surface via a 1-dimensional model (Ref 39). Several parameters can be set for the calculations. These parameters can be divided into several groups: (a) nozzle parameters (nozzle types and injection point), (b) gas parameters (temperature, pressure, gas type and gas composition), (c) injection parameters (fraction of carrier gas, carrier gas temperature and particle injection velocity). In the literature section of the software several publications are listed, divided into the following 6 groups: (i) basics of the calculations of the KSS software (Ref 4, 6, 53), (ii) basics of fluid dynamics in cold spray (Ref 34), (iii) critical velocity and bonding mechanisms in cold spray (Ref 1, 3, 5), (iv) hardening of powder particles (Ref 54), (v) further literature (Ref 55, 56), and (vi) book chapters (Ref 57, 58).

As the KSS software takes the bow shock effect (Ref 59) into account, two different particle velocities, namely max and impact velocities, calculated in the software were considered and compared to the values determined by the IR camera and CSM methods where no bow shock occurred as no substrates were present. For comparison, calculations at a spray distance of 200 mm were performed with the KSS software and the in-flight particle velocities and temperatures at 60 mm downstream the nozzle exit were determined. These calculations were performed since during the experiments no substrate was placed in front of the cold spray gun.

Results and Discussion

Particle Velocity and Temperature—Comparison Between the CSM, High-Speed IR-Camera and KSS Software

In Fig. 3, the measured particle velocities (a, c) and particle temperatures (b, d) of the In718 and TiAlCrNb powder, respectively, are plotted. For the temperature measurement by the IR camera the emissivity of 0.5 to 0.9 for In718 and 0.1 to 0.7 for TiAlCrNb was considered for the analyses. The solid and dashed lines in Fig. 3(b) and (d) are described by Eq 2 (see “Experimental Methods and Data Analysis” section). The data were obtained using a particle diameter of $30 \mu\text{m}$.

Overall the software from Telops identified over 20,000 particles for the selected analysis parameters and each powder. As already mentioned in the experimental section, the analyzed In718-particles were divided into three different classes based on the measured velocity (Fig. 3a, b). In the first group ($v < 400 \text{ m/s}$) 4.1%, in the second group ($400 \text{ m/s} \leq v < 1000 \text{ m/s}$) 84.5%, and in the third group ($v \geq 1000 \text{ m/s}$) 11.4% of the detected particles were found. The average velocity of the slow particles ($< 400 \text{ m/s}$) was 310 m/s. The standard deviation of the particle velocities in fig. a ($400 \leq v < 1000 \text{ m/s}$) is 107 m/s. For the fast particles the standard deviation is much larger (around 300 m/s) and for the slow particle the standard deviation is a little smaller. For the particle temperatures in Fig. 3(b) the standard deviations are around 150°C (for the black points).

An analysis of the individual video frames as shown in Fig. 4(a), (b), and (c) revealed that these slow particles were located at the right or left edge of the field of view of the IR-camera (Fig. 4b, marked by a white arrow). Therefore, only a part of the particle track was visible in the image so that a very low particle velocity was supposed. Moreover, the obtained average particle temperature was low ($T_{\text{average}} = 387\text{--}470^\circ\text{C}$, depending on emissivity), since a smaller area was evaluated and hence a smaller amount of infrared energy was detected by the IR camera. As it can be seen from Fig. 3(b), the fastest particles also possessed the highest temperatures. The average velocity of this group was 1359 m/s and the average particle temperature ranged from 723.9°C ($\varepsilon = 0.9$) to 928°C ($\varepsilon = 0.5$). This observation is also explained in Fig. 4(c). Here, it can be seen that the impression of fast particles is caused by overlapping particle tracks, which is apparent in the presented example since the width of the labeled particle (white arrow in Fig. 4c) changes suddenly. The overlap originates from particles flying at the same height, but at different distances from the camera thus leading to

Fig. 3 Results of the high-speed IR-camera depending on emissivity for In718 and TiAlCrNb: (a) and (c) particle velocities after filtering and (b, d) particle temperatures after filtering, respectively. The calculated particle temperatures for d_{10} , d_{50} , and d_{90} are also presented. The dashed lines are extrapolations of the emissivity dependence of the particle temperature based on Eq 2 in the present work. The data in this figure were obtained using a particle diameter of 30 μm

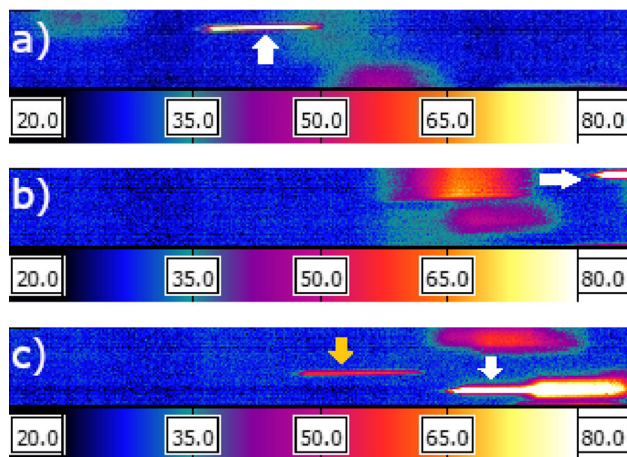
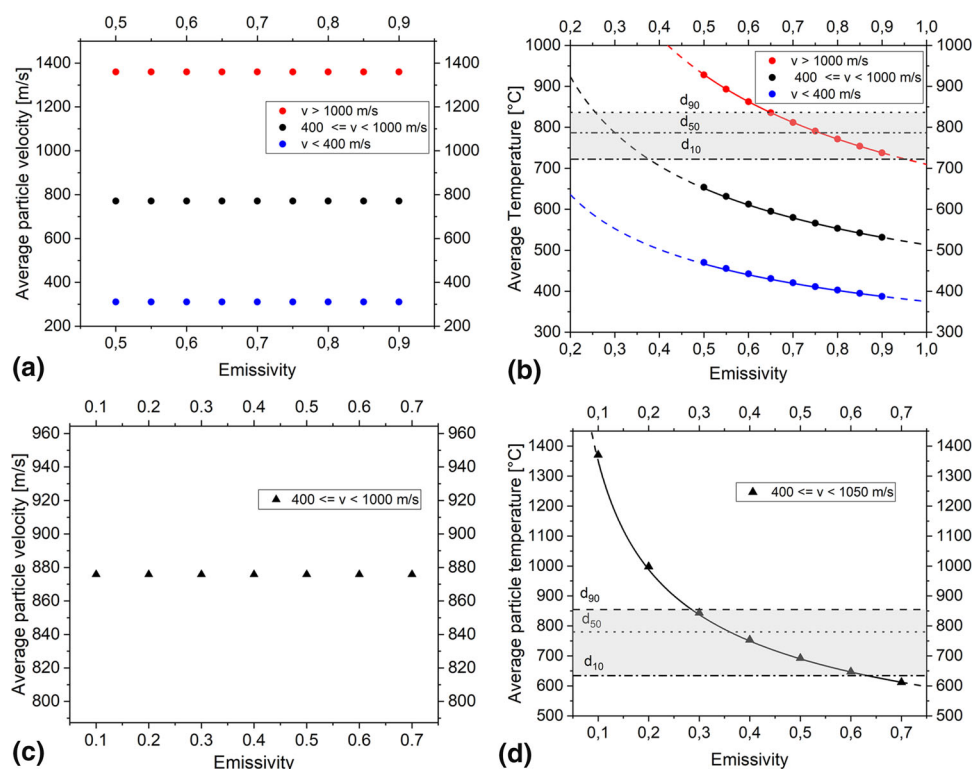


Fig. 4 RAW images of the IR-camera obtained during the measurements with the In718 feedstock at 1100 $^{\circ}\text{C}$ and 50 bar. The color codes represent the temperature of each pixel. Good, partial and overlapping particle tracks are marked by arrows. More details can be found in the text

an overestimation of the particle velocity and the particle temperature, since a larger area is used for the calculations. For the analysis only the “good” particles were considered and examples can be found in Fig. 4(a) (white arrow) and Fig. 4(c) (orange arrow). In Table 1, exemplary values of particle velocities and temperatures (particles in Fig. 4a-c) for an emissivity of 0.7 are listed for the different cases mentioned above. A comparison of the results obtained with the IR camera and a CSM will be discussed later for

Table 1 Particle velocities and temperatures of In718 calculated for the particles visible in Fig. 4(a), (b), and (c). The values for the emissivity (ε) and the particle diameter (d_p) are set in the software

Frame-ID/fig.	ε , Emissivity	d_p , μm	v_p , m/s	T_p , $^{\circ}\text{C}$
693/a (good)	0.7	30	885.9	551.1
17/b (edge)	0.7	30	270.3	551.7
523/c (overlap)	0.7	30	1381.4	1129.7
523/c (good)	0.7	30	931.1	615.8

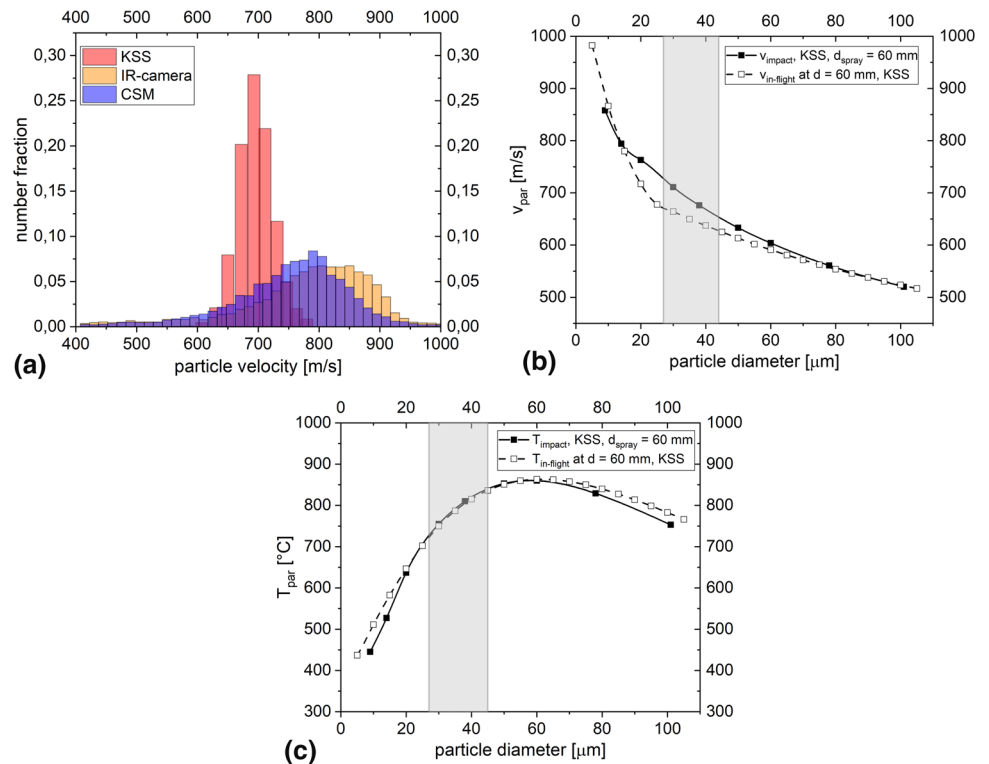
In718, but first the measured particle velocities and temperatures for TiAlCrNb are summarized and evaluated. As the first ($v < 400$ m/s) and third ($v \geq 1000$ m/s) group of particles in In718 data analysis were found to be under- and overestimations stemming from the analysis procedure, only data for the second group ($400 \text{ m/s} \leq v < 1000$ m/s) of particles are shown for TiAlCrNb in Fig. 3(c) and (d). Accordingly, similar to the In718, the particle velocities are independent of emissivity (Fig. 3c) and have an average value of 875 m/s. The average particle temperatures were found to be in the range of 612 $^{\circ}\text{C}$ ($\varepsilon=0.7$) and 1370 $^{\circ}\text{C}$ ($\varepsilon=0.1$) revealing the importance of true emissivity for such thermal measurement. Impact temperatures of 32 μm particles (d_{50}), determined by KSS are given in Table 2. A comparison to IR camera data of 30 μm particles as shown in Fig. 1(d), yields at emissivities between 0.3–0.4 the most comparable results between the two different methods.

Table 2 Results of the KSS software (Ref 39) for the used spray parameters for the d_{10} , d_{50} and d_{90} for the respective powders. The maximum velocity occurs around 2.5 mm in front of the substrate.

Powder	Particle diameter, μm	v_{im} , m/s	T_{im} , $^{\circ}\text{C}$	v_{max} , m/s	η
In718	27 (d_{10})	726	726	735.2	1.47
	35 (d_{50})	689	792	694.4	1.53
	45 (d_{90})	650	841	653.2	1.57
TiAlCrNb	17 (d_{10})	845	603	883	1.23
	32 (d_{50})	773	777	789	1.34
	48 (d_{90})	731	858	740	1.40

Afterward, the box shock effect leads to a slight deceleration of the particles. More details can be found in the text

Fig. 5 (a) Comparison of particle velocity distributions measured with the IR-camera, the CSM, and as predicted by the KSS software using the measured particle size distribution of In718. In (b) and (c) the calculated particle impact velocities and impact temperatures of In718 depending on particle diameter are presented. In addition, the in-flight particle velocities and temperatures are given (details can be found in the text)



A comparison of the particle velocities of In718 measured by IR-camera, CSM and predicted by the KSS software are depicted in Fig. 5(a). The calculations were performed with the KSS software (Ref 39) using the same spray parameters as in the experiments. The left and right edge of the gray box in Fig. 5(b) and (c) represent the d_{10} and d_{90} values of the In718 feedstock, respectively. The in-flight particle temperatures were determined using a spray distance of 200 mm in the KSS and the particle temperatures and velocities 60 mm downstream of the nozzle exit are plotted for comparison. As mentioned in “[Experimental Methods and Data Analysis](#)” section, during the measurements with the CSM, 10,000 particles were detected. To improve the comparison between the results of the CSM and the IR-camera the same filtering method was applied.

Here, 208 particles (2.1%) exhibit a particle velocity of less than 400 m/s and 58 particles (0.6%) fly faster than or equal to 1000 m/s. Overall 9736 particles were analyzed for the velocity distribution in Fig. 5(a) and the comparison between both methods reveals that the IR-camera measurements (Fig. 5a) lead to higher particle velocities. Both distributions are plotted in number fractions. The average particle velocity for the CSM measurement is about 745 m/s and around 770 m/s for the high speed IR-camera. It should be noted that the experimental error for the particle velocities obtained with the IR camera is relatively large which is related to the limited spatial resolution of the images. As mentioned in “[Experimental Methods and Data Analysis](#)” section, the pixel size used for the evaluation is 30 μm . Assuming the minimum inaccuracy of one pixel on

each side of the particle track already leads to an uncertainty of 60 μm for the traveled distance of an individual particle. If the traveled distance is divided by the short exposure time of 2 μs , the resulting minimum error for the particle velocity is 30 m/s. Thus, it can be stated that the results of CSM and IR-camera are in good agreement within the experimental errors.

For the theoretical velocity distribution calculation using the KSS software, the experimentally determined particle size distribution of the In718 powder was considered and for each diameter value the particle impact velocity was calculated. Afterward, the number fraction of each particle size was taken into account and an average velocity was calculated resulting in a predicted value of 696 m/s (Fig. 5a). Overall the impact velocities range from 562 m/s (for particles with 77 μm diameter) to 777 m/s (for particles with 17 μm diameter). A more detailed comparison revealed that approximately 5.5% (CSM) and 6.1% (IR-camera) of the analyzed particles are slower than the predicted 562 m/s, but around 38.4% (CSM) and 57.1% (IR-camera) of the measured particle are faster than the highest predicted velocity of 777 m/s. The KSS software takes the bow-shock effect (Ref 59) into account, but in the experiments no substrate was placed in front of the particle jet, so that no bow-shock effect occurred. Mainly, fine particles are influenced by the shock-waves in front of the substrate reducing the impact velocity. In addition to the impact velocities and impact temperatures the KSS software also enables to analyze the particle velocities and particle temperatures along the entire particle track, in this case the nozzle axis. The maximum particle velocity (V_{max}) occurs at a short distance, approximately 2.5 mm, in front of the substrate. At this distance the KSS software starts to take the bow shock effect (Ref 59) into account. In the software the effect is realized by an abrupt change of the gas velocity down to 50 m/s, which stays constant until the particle hits the substrate. Consequently, the bow shock effect leads to a deceleration of the particles, in particular for particles with a diameter of less than 20 μm . Some examples can be found in Table 2 for the d_{10} , d_{50} and d_{90} -values of the used feedstocks. A more pronounced reduction in particle velocities due to bow shock effect can be seen for TiAlCrNb feedstock in contrast to the In718. This can be attributed to smaller d_{10} value of TiAlCrNb feedstock and about two times lower density of TiAlCrNb ($\sim 3.97 \text{ g/cm}^3$) than that of In718 ($\sim 8.19 \text{ g/cm}^3$) meaning lower inertia of the TiAlCrNb particles when compared to same size of In718 particles. If impact velocities of the d_{10} size TiAlCrNb particles calculated by KSS (845 m/s) are compared to particle velocities measured by IR camera (875 m/s assuming a particle diameter of 30 μm , Fig. 1c) it can be seen that KSS yields lower velocity even for the smaller particles. A better comparison of the predicted and

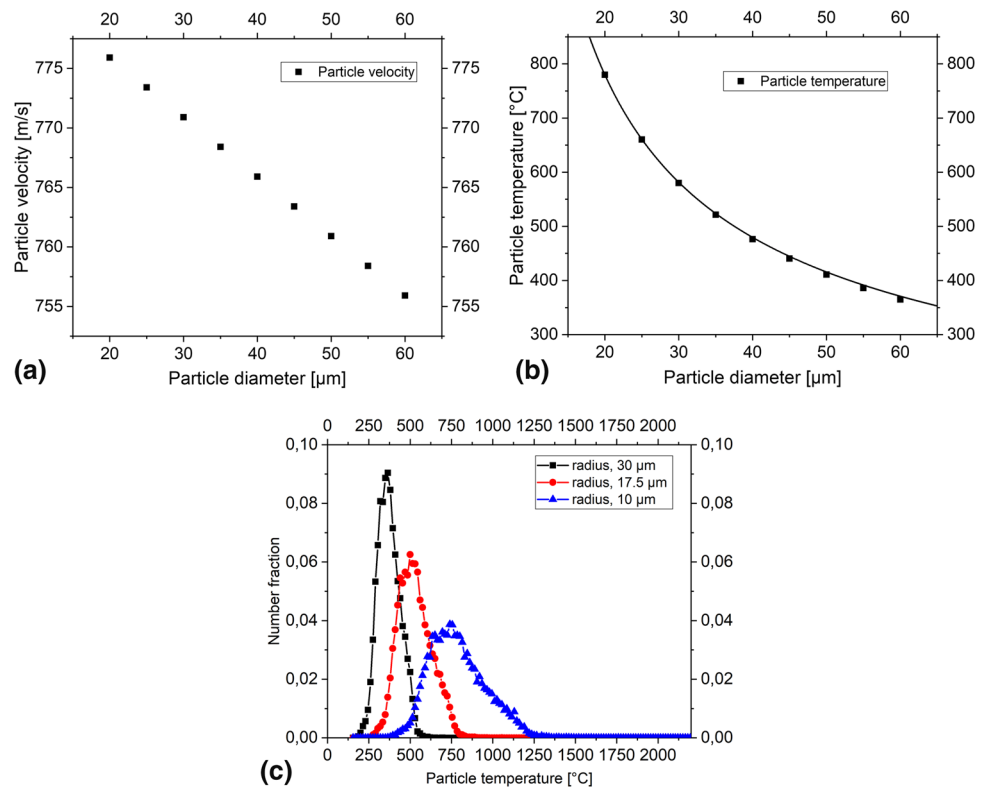
measured particle velocities consequently can be reached when the bow-shock effect is excluded and the maximum particle velocities are considered instead of the impact velocities. A study by Mauer et al. concluded that during CSM measurements corrections for the bow shock effect are reasonable and were found to be larger than predicted by the KSS software (Ref 29). Observed differences between the measured and calculated particle velocities the authors also linked to the powder morphologies which potentially deviated from ideal spheres. Nevertheless, IR camera measured particle velocities still exceed the KSS determined v_{max} values of d_{50} size particles (or d_{10} for IN718) for both materials. It should be noted that the KSS software is using just a 1-dimensional model for the calculations and more precise calculations could be done by CFD simulations.

The drag force acting on the particles depends on several factors, including the drag coefficient. Due to the nature of Newton's law the particle acceleration is proportional to the drag coefficient. The most common expressions for spherical particles used the literature on cold gas spray are the ones of Schiller-Naumann (Ref 60), Alexander and Morsi (Ref 61) and Henderson (Ref 62). As it can be seen in Fig. 1(b), some TiAlCrNb particles show a deviations from the ideal spherical shape. Recently, Ozdemir et al. (Ref 21) investigated the impact of particle shape on measured particle velocities in more detail. In their study, the shape of the feedstock powder was analyzed with a light microscope and significant deviations from the spherical shape were found. The sphericity $\psi = s/S$, first introduced by Wadell (Ref 63) (s = surface area of a spherical particle of equivalent volume, S = surface area of the particle under investigation), is 1 for a perfect sphere and smaller than 1 for all other shapes. Haider and Levenspiel (Ref 64) developed a drag coefficient for non-spherical particles depending on sphericity. Detailed 1-dimensional and 3-dimensional CFD simulations by Ozdemir et al. (Ref 21) for different particle shapes revealed that the discrepancy between the CFS simulations and the velocimetry data originated from the used Schiller-Naumann drag-coefficient (Ref 60) which is valid for spherical particles. A better agreement between theoretical and experimental particle velocities was found using the drag coefficient of Haider and Levenspiel. Since the calculations in the KSS software were performed for spherical particles an underestimation for the particle velocity of non-spherical particles is expected, in particular for TiAlCrNb.

Effect of Particle Size on the Particle Temperature and Velocity

Similar to the influence of emissivity, the effect of the particle size was investigated. In this case, the emissivity is

Fig. 6 Results of the high-speed IR-camera depending on particle size for In718: (a) particle velocities after filtering and (b) particle temperatures after filtering. In figure (c) the influence of the chosen particle size on the temperature distribution is depicted. The solid line in (b) is plotted based on the particle size dependence given in Eq 3 in the present work. The data in this figure were obtained using an emissivity value of 0.7



kept constant and the particle diameter is changed prior to the image analysis with the Telops software. Again, the same particles were analyzed and identified with the software. Due to the change of the particle size, the obtained particle velocity decreases with increasing particle size, as presented in Fig. 6(a). Independently of the particle size, the same area is evaluated in the frames and the travel distance of a particle is calculated between the center of the particle at the start and finish position. Therefore, the total particle track is the sum of two particle radii and the travel distance. As a consequence, the particle velocity decreases by 20 m/s when the particle diameter increases by 40 μm ($40 \mu\text{m}/2 \mu\text{s} = 20 \text{ m/s}$), see Fig. 6(a). To avoid an influence of the velocity filtering process on the results it was decided to use the filtered data set for a particle diameter of 30 μm as a reference. The same particles were analyzed for all the other data sets which were obtained using different particle diameters in the software. If each obtained data set would be filtered individually, some particles with velocities close to the lower (400 m/s) and upper limit (1000 m/s) would be excluded or included in the analyzed data set, respectively, depending on particle size, e.g., a particle with 30 μm diameter and a velocity of 402 m/s in data set A has a velocity of 392 m/s in data set B where a particle diameter of 50 μm was used for the analysis.

Based on Eq 1 a formula linking the temperatures of two particles with the same emissivity but different particle diameters can be derived. Assuming that exactly the same

area of the image (same particle track) is evaluated for different per-set particle diameters leads to the conclusion that the total measured infrared energy is identical. The following relationship can be derived based on this assumption.

$$T_{p2} = \frac{C_4}{\lambda} \left(\ln \left(\frac{R_{p2}^2 \varepsilon}{(1 - \varepsilon) \frac{R_{p1}^2 - R_{p2}^2}{\exp\left(\frac{C_4}{\lambda T_{ref}}\right) - 1} + \frac{R_{p1}^2 \varepsilon}{\exp\left(\frac{C_4}{\lambda T_{p1}}\right) - 1}} + 1 \right) \right)^{-1} \quad (\text{Eq 3})$$

Here, R_{p1} and R_{p2} are the radii of the particles with temperatures T_{p1} and T_{p2} , respectively. The emissivity $\varepsilon = 0.7$, C_4 and λ are constants ($C_4 = hc/k_B = 1.438775 \times 10^{-2} \text{ mK}$ and $\lambda = 4 \mu\text{m}$, see Ref 33). The particle size dependence of In718 according to Eq 3 is plotted as a solid line in Fig. 6(b) and is in good agreement with the experimental data obtained by the image analysis.

As mentioned in “Experimental Methods and Data Analysis” section, for In718 the d_{10} and d_{90} values are 27 and 45 μm, respectively. Within this particle diameter range, the calculated particle temperature decreases from 620 to 440 °C with increasing particle size.

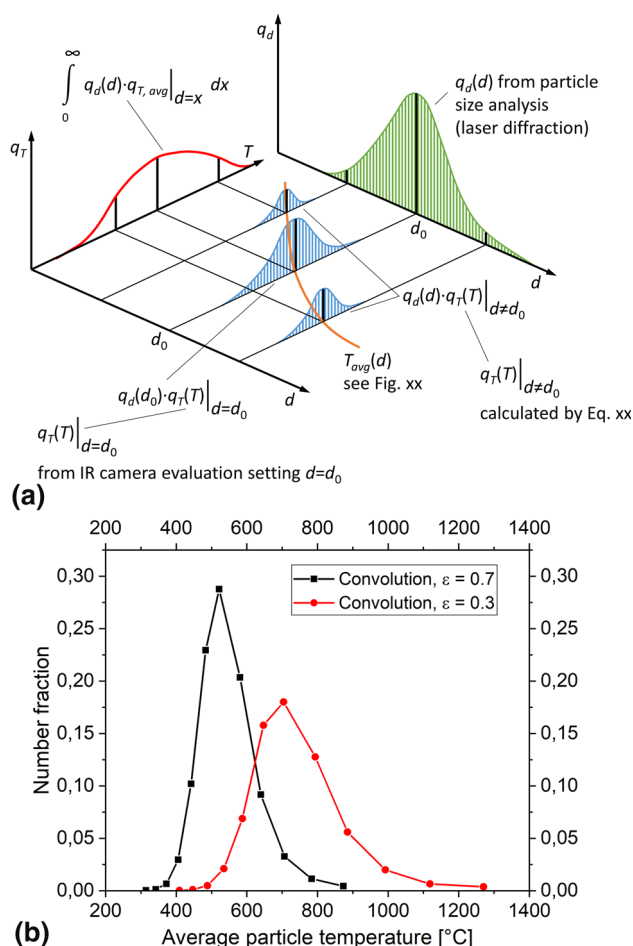


Fig. 7 (a) Schematic description of the approach to analyze the data by convolution, (b) the result of the convolution approach for Inconel 718 feedstock for two different emissivity values

Linking Particle Temperature and Diameter Measurements

As described above, a specific value for the particle diameter d_0 is needed to be used for the evaluation of the measured particle temperatures. Thus, particle diameters must be determined in advance. This can be done, e.g., by the laser diffraction method. A particle sample is suspended in a carrier fluid. A parallel laser beam passing through the suspension flow is scattered at the particles depending on their diameters. The corresponding diffraction patterns are detected and evaluated applying Fraunhofer's or Mie's diffraction theory. Since the particle size in a powder is statistically distributed, the result is a density distribution q_d as a function of the particle diameter d . If this is integrated, the cumulated frequency curve is obtained and some characteristic values like d_{10} , d_{50} , and d_{90} are read to describe the average particle size as well as the width and symmetry of the distribution. The averaged measured particle diameter d_{50} can be used for the initial

evaluation of the measured particle temperatures setting $d_0 = d_{50}$. The result is a density distribution q_T as a function of the particle temperature T . This distribution results from different thermal histories on the one hand and the statistical distribution of the particle diameters on the other hand. However, the temperatures were evaluated with the correct diameter only for particles with $d = d_0$. To improve this situation it is proposed to repeat the temperature evaluation setting different values of the diameter $d \neq d_0$ (this can be easily done using Eq. 3) and to weight the results with the frequency q_d at this value of d in the diameter distribution. Then, these average values of these weighted temperature distributions $q_{T, avg}$ are added up by integration with respect to the temperature T to obtain the particle temperature distribution q_T .

Finally, the resulting temperature distribution q_T is normalized so that its integral with respect to the temperature T is unity. This distribution should represent the effect of the particle size on the particle temperatures in a better way than simply evaluating the temperature measurements setting only one diameter $d_0 = d_{50}$.

For the reference data set used for this method a particle diameter of 30 μm and an emissivity of 0.7 were chosen. By applying Eq 3 the particle temperature distributions were calculated for different particle diameters $d \neq d_0$ considering the experimentally determined particle size distribution, see Fig. 7(b). The obtained temperature distributions were weighted by the number fractions of the particles size distribution (see Fig. 1c) and the average particle temperatures were calculated. The resulting average particle temperature were taken and a new particle temperature distribution was created. This new distribution was normalized and the results are shown in Fig. 7d for two different emissivity values. The influence of the emissivity can be calculated using Eq 2.

Conclusions

The present study is built on the work of Nastic and Jodoin (Ref 33) and represents another step forward toward more accurate in-flight particle temperature measurements during the cold gas spray process. Accurate and reliable particle diagnostics are essential for the development and refinement of models and enable a comparison between the existing theories and experimental observations.

The in-flight measurements of particle temperature and particle velocity with a high-speed IR Camera lead to the following conclusions:

- The measured particle velocity distributions of the CSM and the IR camera are in good agreement with each other considering the larger experimental error of

the IR camera. An increase of 8% (CSM) and 11% (IR camera) compared to the calculated results of the KSS software were found for In718.

- For both materials the experimental results revealed a high dependence of particle temperature on emissivity. For low emissivity values, 0.3 for In718 and 0.3 to 0.4 for TiAlCrNb, the measured particle temperatures are comparable to the predicted temperatures for particles with a diameter of 35 and 32 μm , corresponding to the d_{50} -values of the respective feedstock.

Despite the great progress some challenges remain for the future including further improvements of the camera resolution to distinguish different particle sizes more precisely and to enable better correlation between the measured particle velocities and particle temperatures. Furthermore, it is important to accurately determine the particle emissivity values of the feedstock since the exact value is crucial for the correct calculation of the particle temperatures.

Acknowledgments The outstanding collaboration with the entire team of Telops Infrared Innovations is acknowledged. The team helped with the setup of the experiments and a sophisticated data analysis. Furthermore, Karl-Heinz Rauwald, Doris Sebold and Andrea Hilgers of the Forschungszentrum Jülich are acknowledged for their valuable contributions to the present work.

Funding Open Access funding enabled and organized by Projekt DEAL. Open Access This article is licensed under a Creative Commons Attribution 4.0 International License, which permits use, sharing, adaptation, distribution and reproduction in any medium or format, as long as you give appropriate credit to the original author(s) and the source, provide a link to the Creative Commons licence, and indicate if changes were made. The images or other third party material in this article are included in the article's Creative Commons licence, unless indicated otherwise in a credit line to the material. If material is not included in the article's Creative Commons licence and your intended use is not permitted by statutory regulation or exceeds the permitted use, you will need to obtain permission directly from the copyright holder. To view a copy of this licence, visit <http://creativecommons.org/licenses/by/4.0/>.

References

1. H. Assadi et al., Cold Spraying—A Materials Perspective, *Acta Mater.*, 2016, **116**, p 382-407.
2. M.R. Rokni et al., Review of Relationship Between Particle Deformation, Coating Microstructure, and Properties in High-Pressure Cold Spray, *J. Therm. Spray Technol.*, 2017, **26**(6), p 1308-1355.
3. H. Assadi et al., Bonding Mechanism in Cold Gas Spraying, *Acta Mater.*, 2003, **51**(15), p 4379-4394.
4. T. Schmidt et al., From Particle Acceleration to Impact and Bonding in Cold Spraying, *J. Therm. Spray Technol.*, 2009, **18**(5-6), p 794-808.
5. T. Schmidt et al., Development of a Generalized Parameter Window for Cold Spray Deposition, *Acta Mater.*, 2006, **54**(3), p 729-742.
6. H. Assadi et al., On Parameter Selection in Cold Spraying, *J. Therm. Spray Technol.*, 2011, **20**(6), p 1161-1176.
7. M. Kamaraj and V.M. Radhakrishnan, Cold Spray Coating Diagram: Bonding Properties and Construction Methodology, *J. Therm. Spray Technol.*, 2019, **28**(4), p 756-768.
8. W.-Y. Li et al., Study on Impact Fusion at Particle Interfaces and its Effect on Coating Microstructure in Cold Spraying, *Appl. Surf. Sci.*, 2007, **254**(2), p 517-526.
9. M. Hassani-Gangaraj et al., Adiabatic Shear Instability is Not Necessary for Adhesion in Cold Spray, *Acta Mater.*, 2018, **158**, p 430-439.
10. M. Hassani-Gangaraj et al., In-Situ Observations of Single Micro-Particle Impact Bonding, *Scripta Mater.*, 2018, **145**, p 9-13.
11. D.L. Gilmore, R.C. Dykhuizen, R.A. Neiser, T.J. Roemer and M.F. Smith, Particle Velocity and Deposition Efficiency in the Cold Spray Process, *J. Therm. Spray Technol.*, 1999, **8**, p 576-582.
12. H. Fukanuma et al., In-Flight Particle Velocity Measurements with DPV-2000 in Cold Spray, *Surf. Coat. Technol.*, 2006, **201**(5), p 1935-1941.
13. R.Z. Huang, B. Sun, N. Ohno, and H. Fukanuma, Study on the Influences of DPV-2000 Software Parameters on the Measured Results in Cold Spray, in Thermal Spray 2006: Science, Innovation, and Application (ASM International). 2006.
14. B. Jodoin et al., Effect of Particle Size, Morphology, and Hardness on Cold Gas Dynamic Sprayed Aluminum Alloy Coatings, *Surf. Coat. Technol.*, 2006, **201**(6), p 3422-3429.
15. W. Wong et al., Influence of Helium and Nitrogen Gases on the Properties of Cold Gas Dynamic Sprayed Pure Titanium Coatings, *J. Therm. Spray Technol.*, 2010, **20**(1-2), p 213-226.
16. L. Ajdelsztajn et al., Cold Gas Dynamic Spraying of Iron-Base Amorphous Alloy, *J. Therm. Spray Technol.*, 2006, **15**(4), p 495-500.
17. X. Suo et al., Strong Effect of Carrier Gas Species on Particle Velocity During Cold Spray Processes, *Surf. Coat. Technol.*, 2015, **268**, p 90-93.
18. B. Jodoin, F. Raletz and M. Vardelle, Cold Spray Modeling and Validation using an Optical Diagnostic Method, *Surf. Coat. Technol.*, 2006, **200**(14-15), p 4424-4432.
19. S.P. Pardhasaradhi et al., Optical Diagnostics Study of Gas Particle Transport Phenomena in Cold Gas Dynamic Spraying and Comparison with Model Predictions, *J. Therm. Spray Technol.*, 2008, **17**(4), p 551-563.
20. F. Raletz, M. Vardelle and G. Ezo'o, Critical Particle Velocity Under Cold Spray Conditions, *Surf. Coat. Technol.*, 2006, **201**(5), p 1942-1947.
21. O.Ç. Özdemir, J.M. Conahan and S. Müftü, Particle Velocimetry, CFD, and the Role of Particle Sphericity in Cold Spray, *Coatings*, 2020, **10**(12), p 1254.
22. M. Meyer, S. Yin and R. Lupoi, Particle In-Flight Velocity and Dispersion Measurements at Increasing Particle Feed Rates in Cold Spray, *J. Therm. Spray Technol.*, 2016, **26**(1-2), p 60-70.
23. S. Lange et al., Velocity Diagnostics for Gas Velocity Distributions in Cold Gas and Plasma Spraying Using Non-Resonant Laser Scattering, *J. Therm. Spray Technol.*, 2010, **20**(1-2), p 12-20.

24. H. Koivuluoto et al., Cold-Sprayed Al6061 Coatings: Online Spray Monitoring and Influence of Process Parameters on Coating Properties, *Coatings*, 2020, **10**(4), p 348.
25. A. Sova et al., Visualization of Particle Jet in Cold Spray by Infrared Camera: Feasibility Tests, *Int. J. Adv. Manuf. Technol.*, 2017, **95**(5-8), p 3057-3063.
26. A. Sova et al., Velocity of the Particles Accelerated by a Cold Spray Micronozzle: Experimental Measurements and Numerical Simulation, *J. Therm. Spray Technol.*, 2012, **22**(1), p 75-80.
27. H. Koivuluoto et al., Novel Online Diagnostic Analysis for In-Flight Particle Properties in Cold Spraying, *J. Therm. Spray Technol.*, 2018, **27**(3), p 423-432.
28. H. Tabbara et al., Study on Process Optimization of Cold Gas Spraying, *J. Therm. Spray Technol.*, 2010, **20**(3), p 608-620.
29. G. Mauer et al., Diagnostics of Cold-Sprayed Particle Velocities Approaching Critical Deposition Conditions, *J. Therm. Spray Technol.*, 2017, **26**(7), p 1423-1433.
30. E. Sansoucy et al., Mechanical Characteristics of Al-Co-Ce Coatings Produced by the Cold Spray Process, *J. Therm. Spray Technol.*, 2007, **16**(5-6), p 651-660.
31. P. Richer et al., CoNiCrAlY Microstructural Changes Induced During Cold Gas Dynamic Spraying, *Surf. Coat. Technol.*, 2008, **203**(3-4), p 364-371.
32. E. Sansoucy et al., Properties of SiC-Reinforced Aluminum Alloy Coatings Produced by the Cold Gas Dynamic Spraying Process, *Surf. Coat. Technol.*, 2008, **202**(16), p 3988-3996.
33. A. Nastic and B. Jodoin, Evaluation of Heat Transfer Transport Coefficient for Cold Spray Through Computational Fluid Dynamics and Particle In-Flight Temperature Measurement Using a High-Speed IR Camera, *J. Therm. Spray Technol.*, 2018, **27**(8), p 1491-1517.
34. T. Stoltenhoff, H. Kreye and H.J. Richter, An Analysis of the Cold Spray Process and its Coatings, *J. Therm. Spray Technol.*, 2002, **11**(4), p 542-550.
35. S. Yin et al., Numerical Investigations on the Effect of Total Pressure and Nozzle Divergent Length on the Flow Character and Particle Impact Velocity in Cold Spraying, *Surf. Coat. Technol.*, 2013, **232**, p 290-297.
36. S. Yin et al., Gas Flow, Particle Acceleration, and Heat Transfer in Cold Spray: A review, *J. Therm. Spray Technol.*, 2016, **25**(5), p 874-896.
37. H. Katanoda, Numerical Simulation of Temperature Uniformity within Solid Particles in Cold Spray, *J. Solid Mech. Mater. Eng.*, 2008, **2**(1), p 58-69.
38. R.N. Raoelison, M.R. Guéchi and E. Padayodi, In-Flight Temperature of Solid Micrometric Powders During Cold Spray Additive Manufacturing, *Int. J. Therm. Sci.*, 2020, **157**, p 106422.
39. <https://kinetic-spray-solutions.com/kssapp/kss/home/index.xhtml>.
40. B.P. Keller et al., Total Hemispherical Emissivity of INCONEL 718, *Nucl. Eng. Des.*, 2015, **287**, p 11-18.
41. L. del Campo et al., Emissivity Measurements on Aeronautical Alloys, *J. Alloy. Compd.*, 2010, **489**(2), p 482-487.
42. S. Alaruri, L. Bianchini and A. Brewington, Effective Spectral Emissivity Measurements of Superalloys and YSZ Thermal Barrier Coating at High Temperatures Using a 1.6 μ m Single Wavelength Pyrometer, *Optics Lasers Eng.*, 1998, **30**, p 77-91.
43. G.A. Greene, C.C. Finfrock and T.F. Irvine, Total Hemispherical Emissivity of Oxidized Inconel 718 in the Temperature Range 300-1000 °C, *Exp. Thermal Fluid Sci.*, 2000, **22**(3-4), p 145-153.
44. C.E. Leshock, J.N. Kim and Y.C. Shin, Plasma Enhanced Machining of Inconel 718: Modeling of Workpiece Temperature with Plasma Heating and Experimental Results, *Int. J. Mach. Tools Manuf.*, 2001, **41**(6), p 877-897.
45. G. Pottlacher et al., Thermophysical Properties of Solid and Liquid Inconel 718 Alloy, *Scand. J. Metall.*, 2002, **31**(3), p 161-168.
46. C. Cagran et al., Normal Spectral Emissivity of the Industrially Used Alloys, NiCr20TiAl, Inconel 718, X2CrNiMo18-14-3 and Another Austenitic Steel at 684.5 nm, *Int. J. Thermophys.*, 2009, **30**(4), p 1300-1309.
47. J. Rogers and D. Crandall, Ultra-High Temperature Emittance Measurements for Space and Missile Applications. In National Space & Missile Materials Symposium. 2009.
48. L. González-Fernández et al., Normal Spectral Emittance of Inconel 718 Aeronautical Alloy Coated with Ytria Stabilized Zirconia Films, *J. Alloy. Compd.*, 2012, **513**, p 101-106.
49. V.C. Raj and S.V. Prabhu, Measurement of Surface Temperature and Emissivity of Different Materials by Two-Colour Pyrometry, *Rev. Sci. Instrum.*, 2013, **84**(12), p 124903.
50. P. Skubisz and P. Micek, Determination of Emissivity Characteristics for Controlled Cooling of Nickel-Alloy Forgings, *Solid State Phenom.*, 2013, **208**, p 1-7.
51. E.A. Belskaya, Emissivity and Electrical Resistivity of Titanium Alloys with Aluminum and Vanadium, *High Temp.*, 2012, **50**(4), p 475-478.
52. S. Krishnan et al., Optical Properties and Spectral Emissivities at 632.8 nm in the Titanium-Aluminum System, *Metall. Trans. A*, 1993, **24**(1), p 67-72.
53. T. Schmidt et al., Erratum to: From Particle Acceleration to Impact and Bonding in Cold Spraying, *J. Therm. Spray Technol.*, 2009, **18**(5-6), p 1038-1038.
54. H. Assadi et al., Determination of Plastic Constitutive Properties of Microparticles Through Single Particle Compression, *Adv. Powder Technol.*, 2015, **26**(6), p 1544-1554.
55. K. Binder et al., Influence of Impact Angle and Gas Temperature on Mechanical Properties of Titanium Cold Spray Deposits, *J. Therm. Spray Technol.*, 2010, **20**(1-2), p 234-242.
56. Z. Arabgol et al., Influence of Thermal Properties and Temperature of Substrate on the Quality of Cold-Sprayed Deposits, *Acta Mater.*, 2017, **127**, p 287-301.
57. T. Klassen, F. Gartner, and H. Assadi, Process Science of Cold Spray. High Pressure Cold Spray: Principles and Applications, p. 17-66.
58. H. Assadi, F. Gartner, and T. Klassen, High Pressure Cold Spray: Principles and Applications, p. 67-106.
59. J. Pattison et al., Standoff Distance and Bow Shock Phenomena in the Cold Spray Process, *Surf. Coat. Technol.*, 2008, **202**(8), p 1443-1454.
60. L.N. Schiller, Über die grundlegenden Berechnungen bei der Schwerkraftaufbereitung, *Vdi Zeits*, 1933, **77**, p 318-320.
61. S.A. Morsi and A.J. Alexander, An Investigation of Particle Trajectories in Two-Phase Flow Systems, *J. Fluid Mech.*, 2006, **55**(02), p 193.
62. C.B. Henderson, Drag Coefficients of Spheres in Continuum and Rarefied Flows, *AIAA J.*, 1976, **14**(6), p 707-708.
63. H. Wadell, The Coefficient of Resistance as a Function of Renoylds Number for Solids of Various Shapes, *J. Frankl. Inst.*, 1934, **217**(4), p 459.
64. A. Haider and O. Levenspiel, Drag Coefficient and Terminal Velocity of Spherical and Nonspherical Particles, *Powder Technol.*, 1989, **58**(1), p 63-70.

Publisher's Note Springer Nature remains neutral with regard to jurisdictional claims in published maps and institutional affiliations.